Experiments on the structure and dynamics of forced, quasi-two-dimensional turbulence

By S. NARIMOUSA[1], T. MAXWORTHY[2]† AND G. R. SPEDDING[2]

[1] University of Southern California, Department of Mechanical Engineering,
Los Angeles, CA 90089-1453, USA

[2] University of Southern California, Departments of Aerospace and Mechanical Engineering,
Los Angeles, CA 90089-1191, USA

Simulated upwelling fronts have been generated around the outer edge of a cylindrical tank filled with a two-layer fluid system and driven by a surface stress. Initially, an axisymmetric front was observed which subsequently became unstable to small baroclinic eddies. These eddies continued to grow until they reached an equilibrium size. Under some circumstances, cyclonic eddies pinched-off from the fully developed front and moved away from the mean position of the front into the fluid interior. Streak photographs of the fully developed flow field were digitized to generate a velocity field interpolated on to a regular grid. A direct two-dimensional Fourier transform was performed on the turbulent kinetic energy field deduced from such images and one-dimensional energy $E(k)$ spectra were extracted. Consistent $k^{-\frac{5}{3}}$ energy spectra were found at lower wavenumber, k, and approximately $k^{-5.5}$ spectra at higher k. In any given experiment, the two spectral slopes meet close to a wavenumber $k_w = 2\pi/\lambda_w$ (where λ_w is the mean diameter of a frontal eddy and k_w is the associated wavenumber). According to classical theories, k_w would be the input wavenumber, and the range of k with a $k^{-\frac{5}{3}}$ spectrum would correspond to an inverse energy cascade range; this yielded a Kolmogorov constant (C) that varied within the limits $2.8 \leqslant C \leqslant 3.8$. The approximately $k^{-5.5}$ range, which is much steeper than that predicted by the original statistical theories, is nevertheless consistent with those found frequently in numerical experiments.

The spectral slopes inferred from particle dispersion methods and from one-dimensional Fourier transforms of the longitudinal velocity correlations were compared with the results obtained above and in previous laboratory experiments. In general, the global energy spectra are consistent with an interpretation of the fluid dynamics as being that of two-dimensional turbulence. This in turn implies that known properties of such flows may be invoked to explain the appearance of a number of naturally occurring phenomena in coastal upwelling fronts.

1. Introduction

Satellite (IR) images have revealed meso-scale eddy structures at and in the vicinity of oceanic fronts (upwelling fronts), oceanic currents (the Gulf Stream), and more recently in the open ocean. As in the ocean, sharp-surfaced density fronts have

been produced and investigated in the laboratory (Griffiths & Linden 1981, 1982; Narimousa & Maxworthy 1987a). It has been found that soon after they form, the fronts become unstable to short baroclinic instabilities (waves), which grow in time until they reach a saturated size. Further development of these instabilities cause the fully developed frontal eddies to pinch off and produce isolated coherent vortices in the vicinity of the main front. This collection of frontal eddies combined gives rise to a velocity field that might be described in the language of two-dimensional or geostrophic turbulence.

1.1. *Upwelling phenomena in the laboratory and in the ocean*

One important motivation that triggered this study were observations of thin, long offshore-extending, cold filaments in satellite (IR) images taken off the west coast of the USA during coastal upwelling episodes (Narimousa & Maxworthy 1989). Intense turbulent jets or rivers, which are believed to transport the cold upwelled water far offshore, have been recognized as a possible source for generating these filaments. Narimousa & Maxworthy (1985, 1986, 1987a, b) observed in the laboratory that the turbulent jets were often associated with offshore eddies which could be generated in a variety of ways: (a) large-amplitude instability of standing waves generated by coastal perturbations; (b) large-amplitude baroclinic instability of the front itself and (c) production of eddies due to the presence of an offshore curl in the surface stress. In all cases interaction between the offshore eddies produced the offshore jets, which then transported the upwelled water offshore. If the structure of such an eddy field obeys the laws of two-dimensional or geostrophic turbulence, then the intense turbulent rivers which seem to thread through such eddy fields are responsible for transport of material across it and must be characteristics of such fields.

1.2. *Statistical theories of two-dimensional turbulence*

The early studies of two-dimensional turbulence were concerned with the dynamics of atmospheric meso- and large-scale eddies, which were thought to have two-dimensional structure. In the case of three-dimensional turbulence, Kolmogorov's (1941) cascade hypothesis indicated an equilibrium inertial subrange in which kinetic energy cascaded from low to higher wavenumber (k), and the energy spectra took the form $E \sim k^{-\frac{5}{3}}$. In the case of two-dimensional turbulence there is a second constant of motion, called the enstrophy, which was defined as half of the squared vorticity $\frac{1}{2}\omega^2$. This led Kraichnan (1967) and Leith (1968) to propose both a direct enstrophy and an inverse energy cascade inertial range for the case of forced two-dimensional turbulence. They found that $E \sim k^{-\frac{5}{3}}$ in the inertial range in which energy was transferred to lower k (an inverse cascade), and an $E \sim k^{-3}$ inertial range in which enstrophy moved to higher k. Batchelor (1969) found the k^{-3} range for the case of a freely decaying two-dimensional turbulence, consistent with Kraichnan's and Leith's energy spectrum for the enstrophy cascade range. Studies of three-dimensional, quasi-geostrophic turbulence (Charney 1971; Salmon 1978; Herring 1980; Heyer & Sadourny 1982) indicated the existence of two inertial ranges, k^{-3} and $k^{-\frac{5}{3}}$, which was similar to the spectral characteristics of two-dimensional turbulence. (See also Lesieur 1987 for a comprehensive review.)

1.3. *Numerical simulations*

Besides the early computations of Lilly (1969, 1971, 1972), other numerical simulations of two-dimensional isotropic turbulence have frequently produced energy spectra considerably steeper than k^{-3} in the so-called enstrophy cascade range

(see Deem & Zabusky 1971; Fox & Orszag 1972; Herring *et al.* 1974; Fornberg 1977; Basdevant *et al.* 1981; Bennett & Haidvogel 1983; Haidvogel & Keffer 1984; McWilliams 1984). Herring *et al.* (1974), however, have recognized that very high resolution is required in numerical simulations in order to obtain a proper inertial range at higher wavenumbers. For grid resolutions respectively of 1024^2 and 2048^2 Brachet, Meneguzzi & Sulem (1986) and Brachet *et al.* (1988), observed a k^{-4} slope for a short time, which then rapidly changed to a k^{-3} slope for a more mature flow. Based on the isovorticity contours, they identified the initial regime (k^{-4} slope) to be associated with isolated, discontinuous vorticity-gradient sheets in the turbulent field, as hypothesized by Saffman (1971), who predicted such a spectral slope. The second regime (k^{-3} slope) corresponded to a maximum enstrophy dissipation period, which was the basis for the classical enstrophy cascade hypothesis resulting in the k^{-3} slope. Brachet *et al.* (1988) showed that at later times the vorticity-gradient layers would dissipate and coherent vortices associated with isolated concentrations of vorticity which last for a long time would dominate. This later case was investigated by McWilliams (1984) where such coherent vortex structure was associated with an energy spectrum closer to k^{-5}. More recent numerical simulations (Santangelo, Benzi & Legras 1989) have shown, however, that the value of the final spectral slope is quite sensitive to the shape of the initial energy spectrum.

1.4. *Quantitative experiments*

Field measurements of large-scale atmospheric turbulence have tended to produce energy spectra scaling closer to the k^{-3} law (e.g. Julian *et al.* 1970; Kao, Jenne & Sagendolf 1970; Morel & Larcheveque 1974; Dubois 1975), while others have reported $k^{-\frac{5}{3}}$ inertia range (e.g. Brown & Robinson 1979; Gage 1979; Nastrom & Gage 1983). Measurements of freely decaying two-dimensional turbulence in the laboratory produced an energy spectra with slopes close to $\sim k^{-2.5}$ (Griffiths & Hopfinger 1984; Mory & Hopfinger 1986; Maxworthy, Caperan & Spedding 1987) at higher k, when the dispersion of particle pairs was used as the diagnostic tool. However, recent studies (summarized in Maxworthy 1989) have shown that such methods are in error when the actual spectral slope is larger than -3. In this case Babiano, Basdevant & Sadourny (1985) and Bennett (1984) argue that the lower spectral slopes found by particle dispersion methods were due to non-locality of the particle dynamics while the arguments which lead to the classical relationship between particle diffusion and spectral slope is based on local dynamics.

1.5. *A laboratory model for forced, two-dimensional turbulence*

In the present study, the experiments of Narimousa & Maxworthy (1987a) were employed to investigate the structure of mesoscale turbulence generated via baroclinic instabilities at upwelling fronts. Since the flow field was maintained by a constant supply of energy (see §3), the turbulent flow was forced. As mentioned above, when Mory & Hopfinger (1986), Maxworthy *et al.* (1987) and Narimousa, Maxworthy & Spedding (1987) employed the same particle dispersion methods as Griffiths & Hopfinger (1984), the spectral slopes at higher k were almost identical. It appeared that, independent of the two-dimensional turbulence generation mechanism in the laboratory, the measured spectral slope was always close to $\sim k^{-2.5}$, if particle dispersion methods were used. This result was found to be independent of the number of particles, and considerable changes in values of turbulent Reynolds number or rotation rate (Maxworthy *et al.* 1987; Narimousa *et al.* 1987). Here, alternative attempts to measure the energy spectra $E(k)$ in the instantaneous flow

Experiment	Ω (s^{-1})	$\Delta\Omega$ (s^{-1})	h_0 (cm)	$\partial\rho$ (g/cm^3)	u_* (cm/s)	λ_s(cm)	θ_*	δt (s)
a	2.27	0.185	2.60	0.018	0.36	17.0	1.7	0.5
b	1.50	0.170	2.60	0.020	0.35	11.8	4.0	0.5
c	1.20	0.143	2.35	0.020	0.33	8.5	7.5	0.5
d	0.97	0.130	2.55	0.020	0.35	6.7	11.0	1.0
e	0.85	0.114	2.35	0.020	0.32	4.4	20.0	1.0

TABLE 1. Parameter values for the experiment of Narimousa & Maxworthy (1987a). Here Ω is the tank rotation rate, $\Delta\Omega$ is the differential rotation of the top disc, h_0 is the depth of the top layer, $\delta\rho$ is the density difference between the two layers, u_* is the applied friction velocity, λ_s is the final width of the upwelled water at the surface, $\theta_* = (g'h_0)/(u_* f\lambda_s)$ (where $g' = g\delta\rho$ and $f = 2\Omega$ is the Coriolis parameter) is the fundamental controlling parameter of this system and δt is the exposure time for the streak photograph.

field are reported. Fourier transforms of either the two-point velocity correlations or directly on the two-dimensional kinetic energy fields provided two measures of $E(k)$ which could be compared with theoretical, numerical and experimental values previously reported in the literature and with each other.

2. The experiment

Since the present study employs the experiments of Narimousa & Maxworthy (1987a), the reader is referred to that paper for a detailed discussion of the apparatus and the range of parameters used, and only a brief description will be given here.

Two layers of salt water of slightly different densities were brought to solid-body rotation inside a cylindrical tank (90 cm in diameter and 20 cm in depth) having a conical bottom with a slope of about 0.27. The surface of the upper fluid was in contact with a circular, smooth disk, which, as it rotated, applied a stress to this surface producing an alongshore shear flow and an offshore Ekman flux in the top layer. As a result, an upwelling front was formed around the outer edge of the tank. The velocity vectors of the current and the upwelling frontal movement were observed by placing small neutrally buoyant particles in the front and recording their motion by steak photography. The direction of motion of these particles were found by firing an electronic flash at the beginning of the time exposure. To reveal the structure of the eddies, the camera was set to rotate at a rate close to the drift velocity of the eddies. In this way a frozen velocity field was recorded and the resulting streaks represented the turbulent velocities.

In the present study, five experiments with parameter values shown in table 1 below are subject to spectral analysis.

3. Evolution of forced mesoscale turbulence

When the system was in solid-body rotation, the top disk was set to rotate anticyclonically, thus applying a stress to the top surface of the lighter fluid. The resulting Ekman flux caused the top layer to spin down and the interface to rise near the wall and to descend at the centre of the tank. The interface continued to rise near the wall until it intersected the top disk and a surface front was formed. This front then migrated away from the wall and allowed bottom water to appear at the surface around the outer edge of the tank. Eventually, the horizontal pressure gradient

caused by front deformation balanced the Coriolis force and the front became stationary at a distance λ_s from the wall of the tank. Prior to this, at a distance $\lambda_1 < \lambda_s$ the upwelling front became unstable to small baroclinic instabilities. During migration of the front, the small disturbances continued to grow until they reached a saturated size λ_w. In this way intense baroclinic eddies of the form of cyclone–anticyclone pairs dominated the sharp-surfaced density front. The distance where the waves first appeared at the front $\lambda_1 \approx 0.7\lambda_s \theta_*^{-0.5}$, and the mean diameter of the saturated waves $\lambda_w \approx 0.15gh_0/u_*f$ were given by Narimousa & Maxworthy (1987 a).

At large values of θ_*, the frontal eddies were large, and they tended to remain at the front and consequently no pinch-off process was observed. Later, however, less intense eddies were formed in the upper layer adjacent to the more intense frontal eddies (figure 1 a). At moderate values of θ_*, frontal eddies were of a smaller size and they were more intense, yet no eddy escaped from the front. Here again, less intense eddies were formed in the upper layer (figure 1 b) just as those seen in flows with large θ_*.

At low values of θ_*, frontal instabilities were much more intense and the upwelling front itself displayed strong unsteadiness. This eventually initiated large-amplitude wave instabilities which usually started at the wave troughs (i.e. the location of the cyclonic eddies) and then grew into the fluid interior. Later, cyclonic eddies were detached from such intrusions to form intense, isolated coherent cyclonic eddies in the top layer (figure 1 c) away from the mean position of the front. Initially, the mean diameter of a pinched-off cyclone was about the same as that of frontal eddies λ_w but they subsequently continued to grow to a large value of about 3–4 times greater than λ_w, (i.e. an inverse energy cascade). Detachment of the cyclonic eddies occurred randomly at different locations of the front. Interactions of the pinched-off cyclones forced intense anticyclones to develop in between them. The pinched-off eddies, in particular, are of special interest in the present study because of their importance in the transport of the material across the turbulent flow field. To illustrate this Narimousa & Maxworthy (1987 a) released a passive marker within the upwelled water near the wall of the tank. The radial Ekman flow transported the marker toward the front where it interacted with the frontal eddies. At the pinched-off eddy, the marker was transported abruptly into the fluid interior by the induced flow. Such demonstrations in the laboratory led to the conclusion that the presence of eddies adjacent to an upwelled water front, for example, can be responsible for the transport of the upwelled water into the eddy field, in the form of long filaments.

We proceed to investigate such flows by means of statistical tools to measure their energy spectra. Such measurements should provide us with the information to show whether or not our model has at least some of the characteristics of two-dimensional turbulence as determined from theoretical and numerical studies.

4. Particle image analysis

4.1. Procedure

A variety of statistical methods may be applied to the frozen turbulent flow represented by streak photographs such as figure 1 (a–c). In these photographs, the beginning of each streak is composed of a bright spot followed by a less bright tail. Provided that particles do not move out of the illuminated region, their length is proportional to their velocity integrated over the exposure time, δt. The practical choice of δt reflects a compromise between upper bounds due to excessive curvature
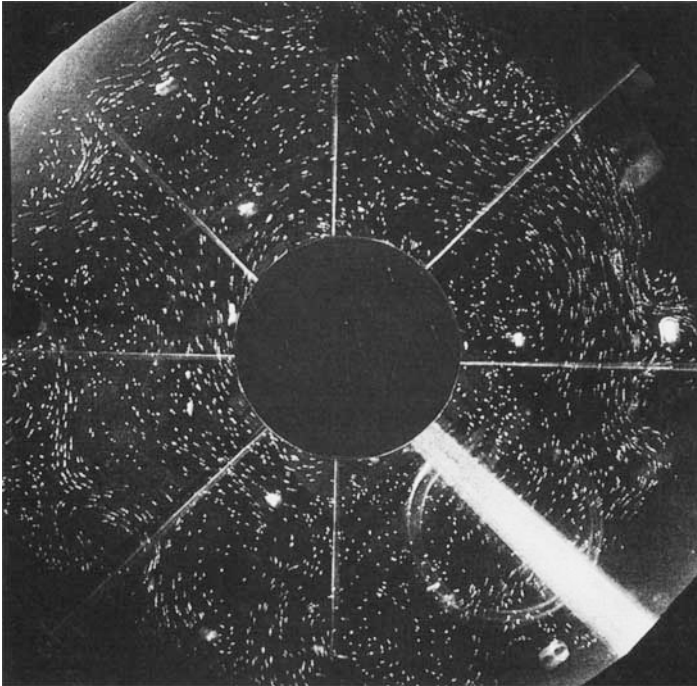
(a)
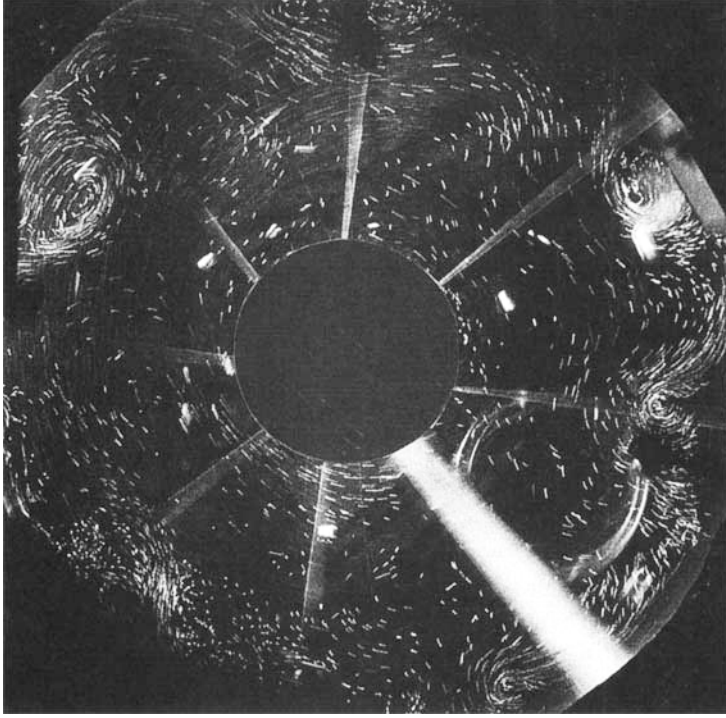
(b)

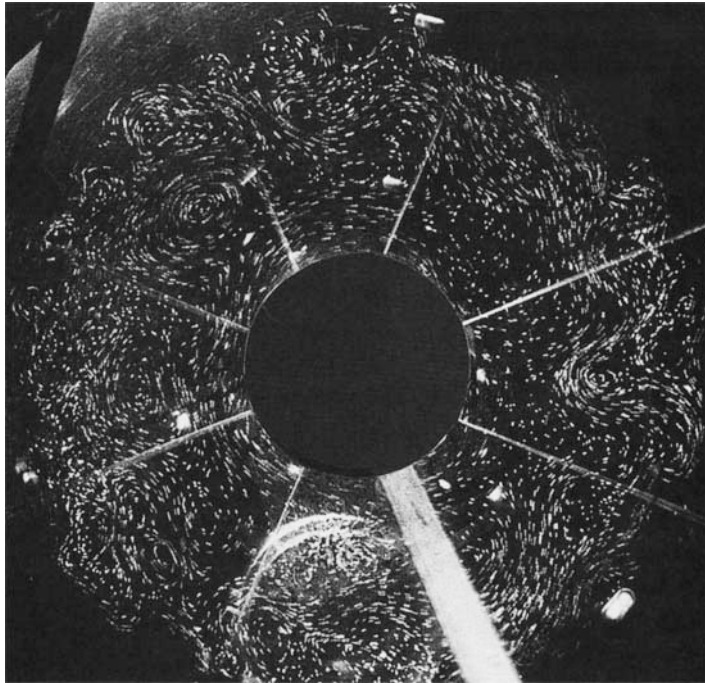FIGURE 1 (a, b). For caption see facing page.

(c)

FIGURE 1. Streak photographs of frozen fields showing examples of the long-time behaviour of meso-scale eddy structures at upwelling fronts and their immediate vicinity. Photographs (a–c) correspond to experiments e, c and a, respectively.

of the particle tracks and lower limits on the detectability of motion in low-speed regions. The exposure times (0.5, 1 s) were determined by the internal timer of a Nikon F2 camera. At these shutter speeds the uncertainty in δt is less than 1%. In each digitized photograph, the end points of 2000–4000 particle streaks were digitized. The irregularly spaced particle velocity data were interpolated on to a 32^2 grid by convolution with an adaptive Gaussian window, as described by Agüí & Jimenez (1987).

4.2. *Error estimates*

The likely sources and magnitudes of the errors in both of these processes have been considered in some detail by Imaichi & Ohmi (1983), Agüí & Jimenez (1987) and Rignot & Spedding (1988). A reasonable error estimate for image digitization is 5%, which is likely to be significantly below the errors introduced by the subsequent interpolation. Rignot & Spedding (1988) presented a detailed comparison between smoothing window-based (adaptive Gaussian window, AGW) interpolations and a thin shell spline (STS) method for the particular case of particle tracking in fluid flows. The magnitude of these errors may be expressed as a function of the characteristic lengthscale of the flow, L, the mean nearest-neighbour distance between particles, δ, and the grid spacing, h. These may be written as the dimensionless ratios L/H and h/δ, which take the values 5 and 2.5 respectively on average in this case. Thus, one might expect *a priori* errors in u and ω of the order of 5 and 10% respectively, according to the simulations of Rignot & Spedding. Bootstrap error estimates on the interpolated u- and ω-fields support this prediction. Clearly the interpolated grid results need to be interpreted with caution. The

accuracy of the AGW technique is not sufficient to determine the details of the shapes of the ω-distributions and the satisfactory h/δ ratio is achieved at the expense of L/h; in other words the resolution at small scales is poor. The highest accessible wavenumber $k \approx \pi$, but values for k several times smaller than this may be suspect. Since values of $k > 1$ are of some interest in this study, an extensive range of grid interpolations were performed, varying the relative grid size, implicit and explicit smoothing parameters and differencing schemes for the AGW interpolation. Comparisons were also made with selected STS and local linear least-squares interpolators. The shape of the global $E(k)$ spectrum below $k \approx 2$ was not affected by changes in the interpolation scheme, nor by small changes in h around the actual values used for the AGW interpolations reported here. By contrast, the tail of the $E(k)$ distribution, for $k > 2$, could be moved almost at will by altering the interpolation parameters. The distributions plotted here appear to lie on linear extrapolations of the data inside $k = 2$, but these values are extremely sensitive to the analysis techniques, and should not be taken as accurate. The estimate of spectral slopes in the enstrophy cascade range must be made from the rather small range of $1 \leqslant k \leqslant 2$. From the comparative and parametric studies of the grid interpolation techniques, the contribution to the uncertainty in assigning an exponent to the energy decay in this region from the interpolation process is approximately ± 0.5.

The seeding particles themselves are neutrally buoyant, and have a mean diameter of approximately 0.83 mm. The minimum resolvable lengthscale, dictated first by the particle density, and second by the grid mesh size, h, is more than an order of magnitude larger than this.

4.3. *Measurements*

The global energy spectrum of each flow field image was estimated in three different ways: (a) relative particle dispersion measurements, (b) two-dimensional Fourier transform of the turbulent kinetic energy field ($\frac{1}{2}u'^2$) on the grid data, and (c) Fourier transforms of the longitudinal two-point turbulent velocity correlation coefficients. There are different assumptions, implicit or explicit, behind each of these techniques which will be discussed in turn. One may note that technique (b) uses the grid-interpolated data, while techniques (a) and (c) do not.

5. Results

5.1. *Method (a)*

Particle dispersion methods were introduced by Morel & Larcheveque (1974) to calculate the energy spectrum of large-scale atmospheric turbulence by observing the relative motion of balloon pairs. Griffiths & Hopfinger (1984) extended this dispersion method, based on a suggestion by one of the present authors, to calculate E from an analysis of streak photographs similar to those of the present study. Briefly, they related the mean-square relative velocities of the particle pairs (or the structure function, Mory & Hopfinger 1986) $\langle (dD/dt)^2 \rangle$, to their separation ($D$) to find

$$\left\langle \left(\frac{dD}{dt} \right)^2 \right\rangle \sim D^{\alpha-1}, \qquad (1)$$

where D is the mean separation of the particle pairs, t is the time and the angle brackets indicate an average over all particle pairs. In (1) the turbulence is assumed
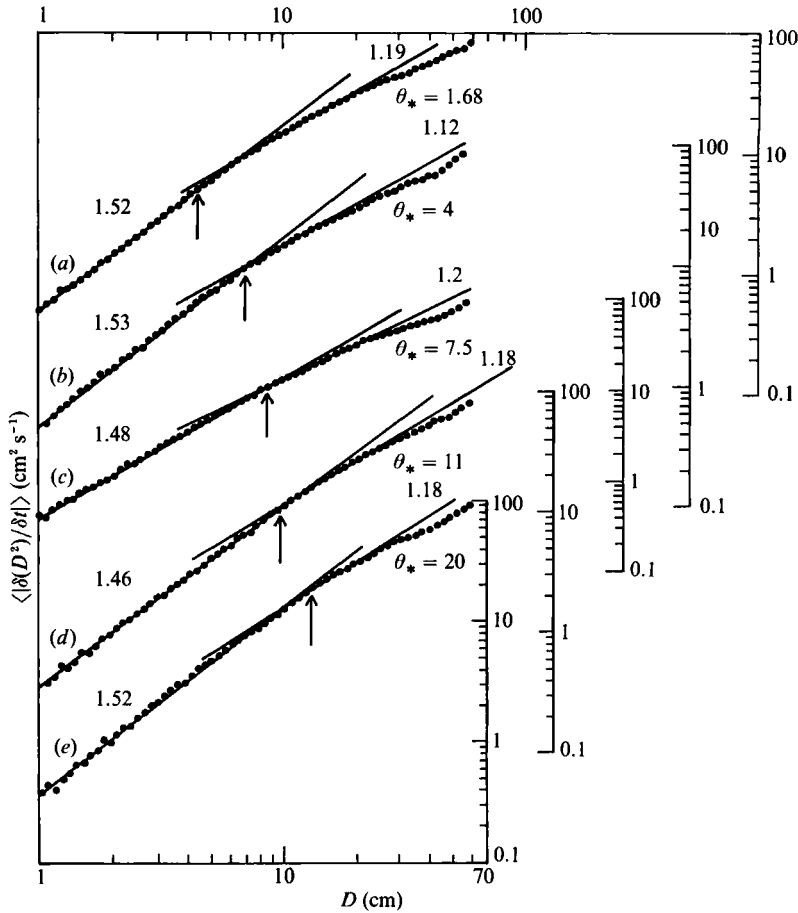
FIGURE 2. Variation of particle dispersion $\langle |\delta D^2/\delta t| \rangle$ with separation D; $(a–e)$ correspond to experiments a–e, respectively. The vertical arrows indicate the wavelength of the frontal eddies. Values of the slopes are indicated.

to be stationary and homogeneous and the energy spectrum takes the form of a simple power law, $E \sim k^{-\alpha}$, where α is an unknown constant to be determined experimentally. A sharp cut-off at some energy dissipation wavenumber and local particle dynamics are assumed in the analysis leading to (1).

The same authors also considered the dissipation rate, or diffusivity of particle pairs $\langle dD^2/dt \rangle$, and since the mean Eulerian value of this quantity over a large number of particle pairs in a two-dimensional flow should be zero, Griffiths & Hopfinger (1984) defined a quadratic diffusivity $\langle |dD^2/dt| \rangle$ and related it to (D) to find

$$\left\langle \left| \frac{dD^2}{dt} \right| \right\rangle \sim D^{\frac{1}{2}(\alpha+1)}. \tag{2}$$

Note that (2) was obtained using the same assumptions used to obtain (1).

In order to obtain α and therefore the form of E, we adopt the data collection technique introduced by Griffiths & Hopfinger (1984). Consider two particles located at initial positions r_1 and r_2 at the beginning of a photographic exposure, and at r_1' and r_2' after time δt, and define the mean separation $D = \frac{1}{2}((r_2'-r_1')+(r_2-r_1))$, the
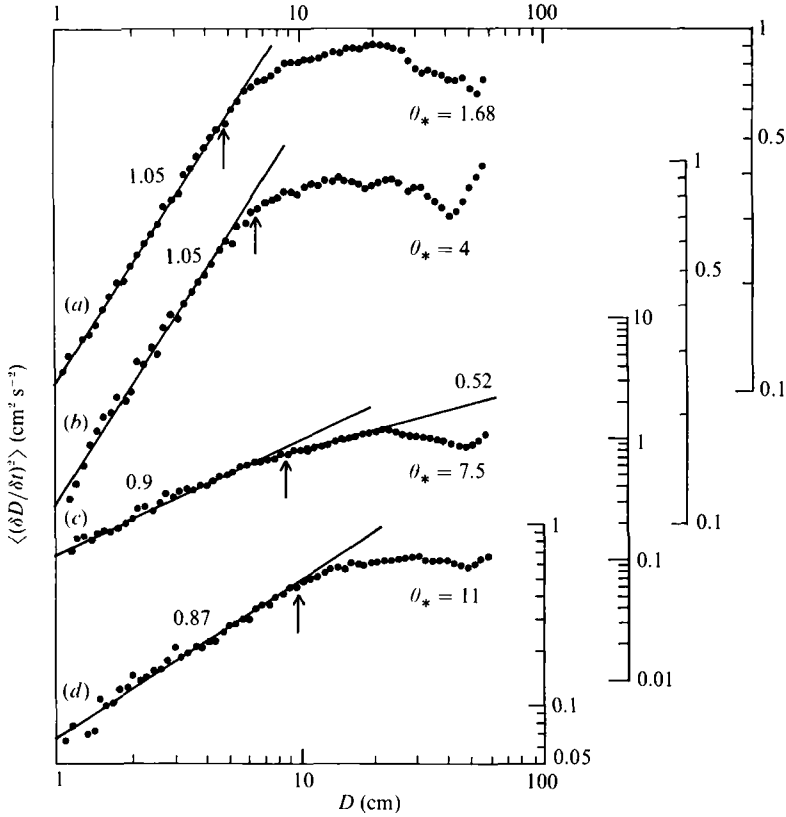
FIGURE 3. Variation to the mean square relative velocity $\langle(\delta D/\delta t)^2\rangle$ with separation D; $(a$–$d)$ correspond to experiments a–d respectively. The arrows are as in figure 2 and values of the spectral slopes are indicated. Note the different vertical scales for (a, b) and (c, d) respectively.

change $\delta D = (r_2' - r_1') - (r_2 - r_1)$ and $\delta(D^2) = 2D\delta(D) = (r_2' - r_1')^2 - (r_2 - r_1)^2$. These quantities may be calculated directly for every particle pair in a given digitized photograph and, given δt, then the left-hand side of (1) and (2) can be calculated for all particle pairs for given separations.

To compute α, the quadratic diffusivity$\langle|\mathrm{d}D^2/\mathrm{d}t|\rangle$ and the structure function $\langle(\mathrm{d}D/\mathrm{d}t)^2\rangle$ are plotted as a function of the separations D in figures 2 and 3 for the five experiments. In general, for each experiment, there appear to be two ranges of D where straight lines may be fitted to the data, and these two lines intersect at a value of $D \approx \lambda_w$. The slopes of these lines, which were fitted by eye, do not vary significantly with θ_*. For $D < \lambda_w$, $\alpha \approx +2$, considerably smaller than the value of $+3$ of classical turbulence results, and smaller still than typical numerical simulation results. When Babiano *et al.* (1985) substituted non-local energy spectra steeper than k^{-3} into the analysis leading to (1), they found that the structure function $\langle(\mathrm{d}D/\mathrm{d}t)^2\rangle$ saturated at D^2, and became independent of the true exponent, α. Their results indicated that (1) is valid only for $1 < \alpha < 3$, and the use of (1) for measurements in the laboratory flows should always give a spectral slope within that range. This may explain why spectral slopes $\alpha \leqslant 3$ were obtained in the present and previous laboratory studies when particle dispersion methods were used.

For wavelengths greater than λ_w, figures 2 and 3 imply that $\alpha \approx +\frac{3}{2}$, less than the $+\frac{5}{3}$ predicted by classical theories for the inverse energy cascade inertia range.
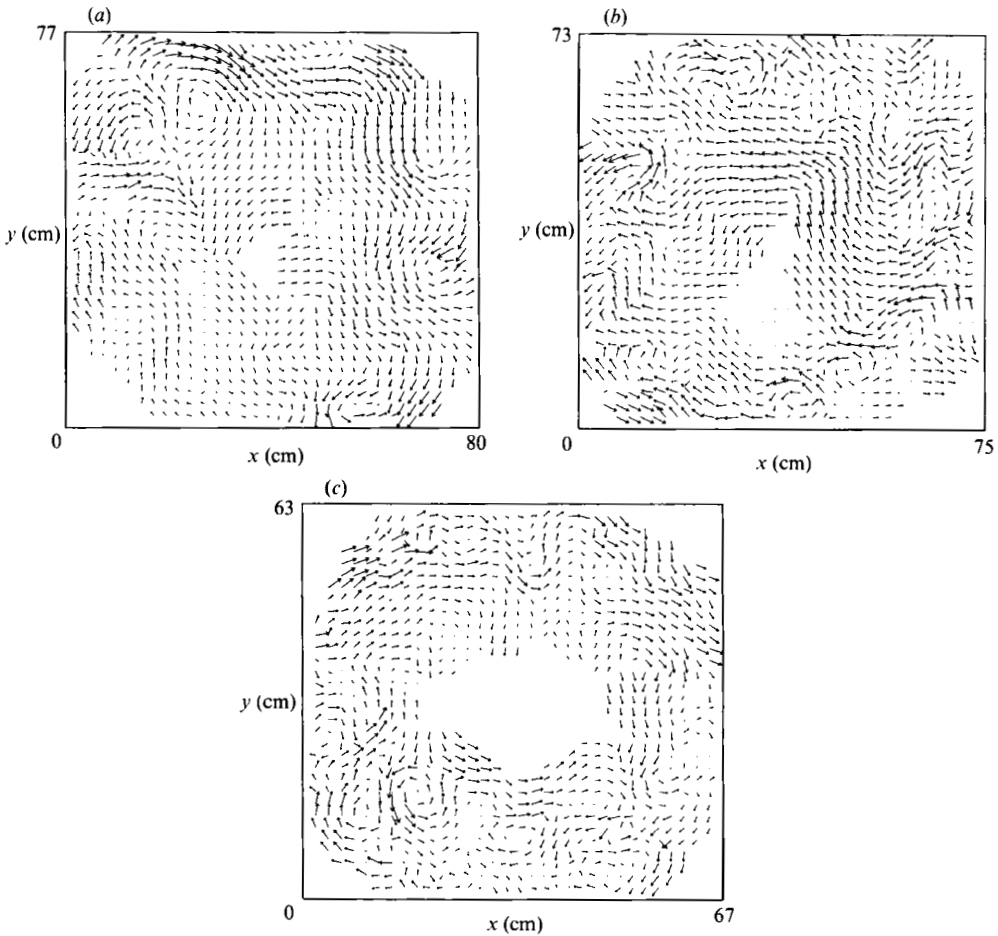
FIGURE 4. The original particle streak data as interpolated on to a regular 32^2 grid by convolution with an adaptive Gaussian window. Here $(a-c)$ correspond to figure 1 $(a-c)$ respectively.

Although this method did not produce the spectral slopes obtained in theories and numerical simulations, it does suggest that the input wavelength is about the same as the mean diameter of the frontal eddies λ_w.

5.2. *Method* (b)

Here, one computes a two-dimensional FFT on the square-grid-interpolated u'^2 field (figure 4). With only a 32×32 resolution in x and y, only a limited range of Fourier coefficients are calculated, and great care must be taken in windowing the data at the edges and centre of the square grid, which has been superimposed on data occupying an annulus-shaped region within its borders. The two-dimensional spectra were collapsed on a one-dimensional transect by adding values around circular shells centred at the origin (kx_0, ky_0). The procedure was similar to that described by Armi & Flament (1985) and their cautionary remarks concerning the interpretation of power spectra should be borne in mind here. Particular care should be taken for the higher values of k, where details of the interpolation, smoothing and windowing techniques may have a significant influence, as discussed in §4.

Once again the $E(k)$ curves (figure 5) appear to be divisable into two regions, each
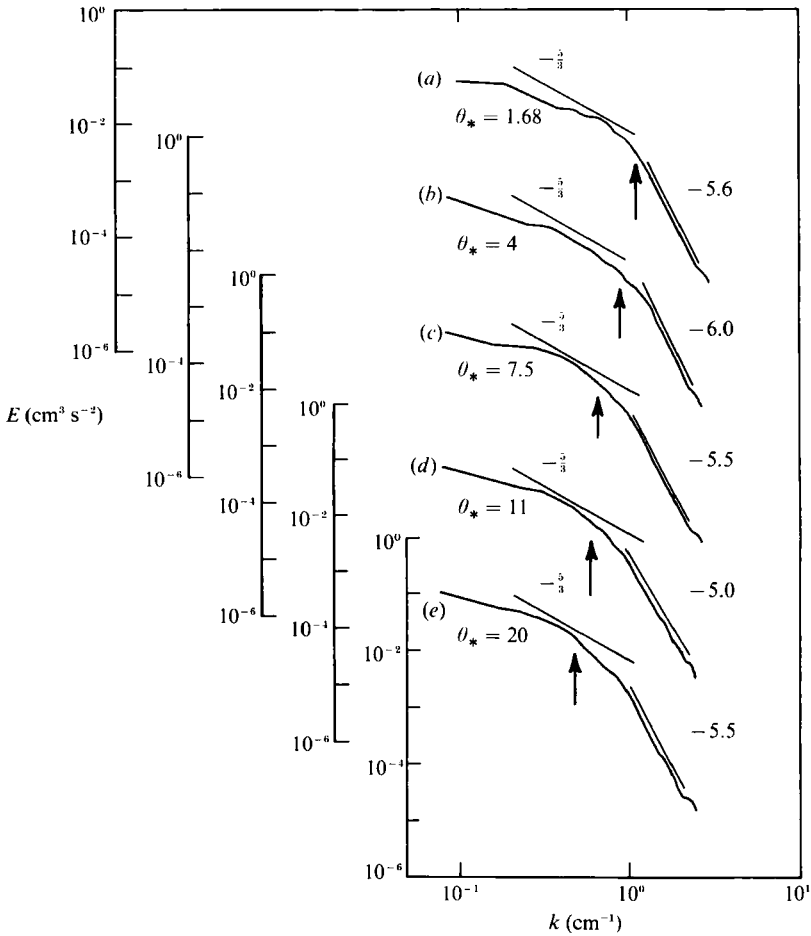
FIGURE 5. One-dimensional energy spectra (e) as a function of wavenumber (k), inferred from a direct two-dimensional, FFT of the u'^2 velocities deduced from the interpolated data such as those shown in figure 4. The labels (a–e) correspond to those in figure 2. Rough estimates of spectral slopes are indicated for each experiment. The vertical arrows indicate the wavenumber of the frontal eddies.

of which may be approximated by a straight line fit (by eye). At low k, the slopes are consistent with a $-\frac{5}{3}$ law; above a relatively well-defined value of k, however, all spectra show a much steeper drop-off, having values of approximately -5.5 for a wide range of values of θ_*.

While the $-\frac{5}{3}$ slopes are quite consistent with the inverse energy cascade described by statistical theory of forced two-dimensional turbulence, the high-wavenumber behaviour differs from the predicted -3 law, in common with results from a number of numerical experiments for both the constant-forcing and the freely decaying cases (e.g. McWilliams 1984; Frisch & Sulem 1984; Herring & McWilliams 1985; Brachet *et al.* 1988) and as found also by Sommeria (1986) for mercury in a closed box in the presence of a strong magnetic field. In general, attention has been focused on the development and subsequent evolution of isolated patches of vorticity which persist for long times and seem to be responsible for exponents steeper than -3. Santangelo *et al.* (1989) have shown that the value of α is actually quite sensitive to the shape of the initial energy spectrum in the freely decaying case and it is reasonable to

suppose that this role might be assumed by the nature of the forcing in the stationary case. Under these circumstances the many different values of spectral slopes reported in the literature are not so surprising. As these authors noted, this sensitivity to initial conditions casts some doubt as to the truly universal nature of two-dimensional turbulence, or at least numerical simulations of it.

In the present study, the recorded turbulent velocity field represents the fully developed, long-time behaviour of the flow (see §3). Figure 6(a–c) shows examples of contour maps of the vorticity field in which many coherent vortex structures can be seen. These structures are closely packed as in Brachet *et al.* (1988) and Santangelo *et al.* (1989) for example, and not isolated as found by McWilliams (1984). Given the nature of the interpolation technique, one is almost guaranteed that the higher-order statistical moments have not converged and only the most general remarks may be made. Having said that, the kurtosis of the vorticity field,

$$k_\omega = \frac{1}{M \times N} \sum_{j-1}^{N} \sum_{i-1}^{M} \left[\frac{\omega_{ij} - \bar{\omega}}{\sigma} \right]^4, \tag{3}$$

is a measure of the flatness of the vorticity distribution ω_{ij} on the $M \times N$ grid array. The mean value was 4.0 over experiments a–e and the maximum value was 4.6. This is far below the values of 10–30 reported by McWilliams (1984) and is more comparable to the value of a Gaussian distribution where $k = 3$. We can make no more precise statements on the shape of the vortices except that they are not isolated and strongly peaked. Nevertheless, we found that such coherent vortex structures can actually produce an approximately $k^{-5.5}$ energy spectrum. This implies that, so far as the long-time behaviour of the flow is concerned, the slope of energy spectra at higher k is always steeper than k^{-3}, regardless of the degree of isolation of the coherent vortices. The fact that the turbulent flow in our laboratory model is forced, rather than freely decaying, may reduce the degree of isolation, as vortices of size λ_w are constantly generated at the front and injected into the system.

If the wavenumber $k_w = 2\pi/\lambda_w$ corresponds to the frequency at which most energy is injected into the flow field then the two spectral slopes for each experiment should meet at this point on the k-axis. Figure 5 shows that this is a plausible interpretation of the data for each of the five different values of θ_*. Since $\lambda_w \sim (g'h_0)/(u_* f)$ is a function of both the Rossby deformation radius $Ro = (g'h_0)^{0.5}/f$ and the Richardson number $Ri = (g'h_0)/u_*^2$, we can write

$$k_w = \frac{2\pi}{\lambda_w} \sim 2\pi \left(\frac{u_* f}{g'h_0} \right) \sim 2\pi \, Ri^{-0.5} Ro^{-1}. \tag{4}$$

Table 2 shows the values of λ_w, Ro, Ri, α (at large k) and θ_* for experiments a–e of figure 5, respectively. This table shows that in any given experiment λ_w is about 3 times greater than Ro. Initially, when the eddies first appear at the front they have a size comparable with Ro, but they continue to grow to a final size λ_w, controlled by θ_*. When the values of λ_w obtained in the present study were compared with those obtained in previous studies of baroclinic turbulence (Phillips 1954; Griffiths & Linden 1982, Chia, Griffiths & Linden 1982; and Killworth, Paldor & Stern 1984) a good agreement was achieved. Under circumstances (figure 1c) when eddies are pinched-off from the front (see §3), their scale increases to values of $\sim 4\lambda_w$ and/or $\sim 12Ro$. At this stage such eddies could be of equivalent-barotropic type (McWilliams 1984). However, Griffiths & Linden (1981) showed that at values of $h_0/H \geqslant 0.25$ (H is the average total depth of the water), which is the case in the present experiments, the generated instabilities are of baroclinic type.
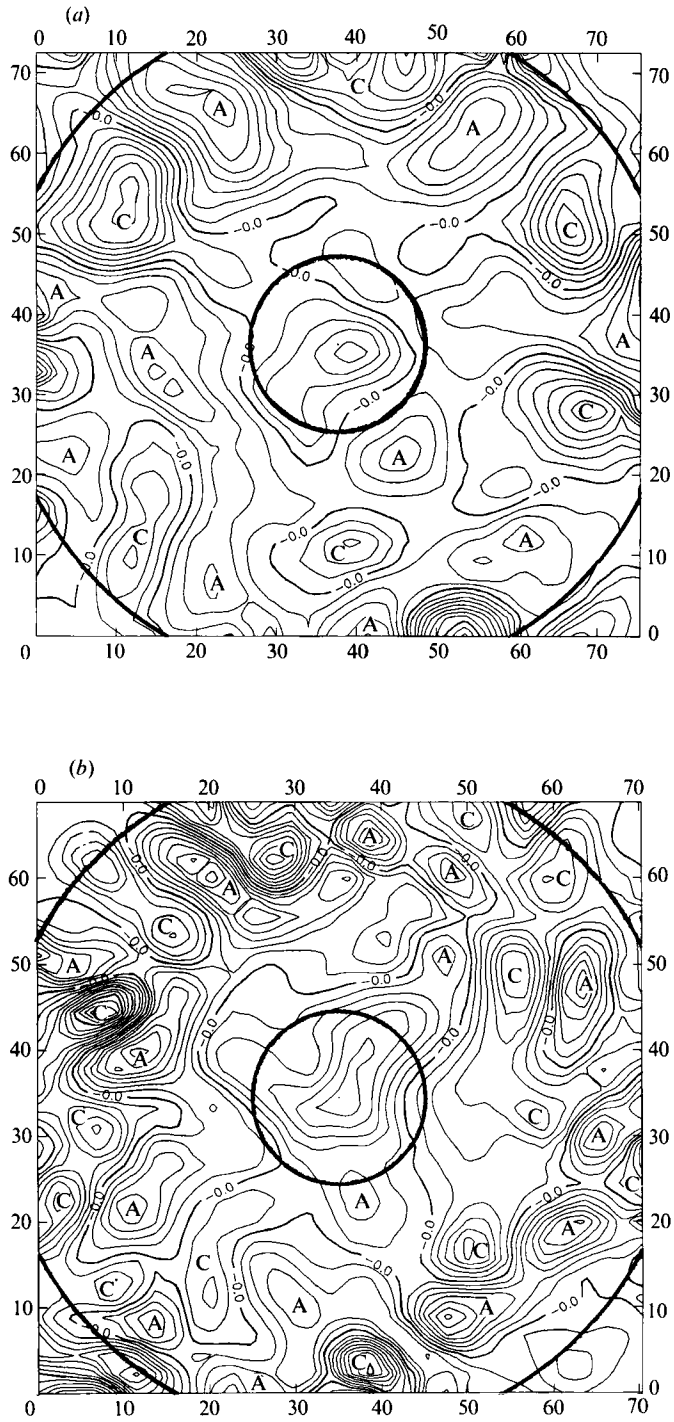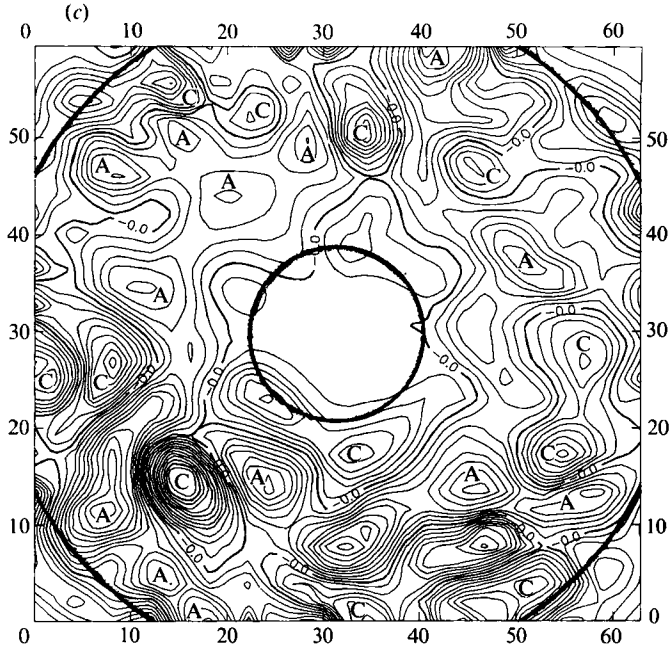
FIGURE 6(*a*,*b*). For caption see facing page.

FIGURE 6. Isovorticity contours for the grids of figure 4. There are 16 contour levels, linearly spaced between ω_{min} and ω_{max}. Contour levels drawn outside the boundaries of the tank (heavy lines) are artifacts of the contouring routine which insists on data on a rectangular grid. The cyclones are indicated by C, while the anticyclones by A.

	λ_w (cm)	Ro	Ri	α	θ_*
a	4.3	1.5	355	-5.6	1.7
b	7.0	2.4	416	-6.0	4.0
c	9.6	2.8	422	-5.5	7.5
d	11.0	3.6	408	-5.0	11.0
e	13.2	4.0	449	-5.5	20.0

TABLE 2.

5.3 *Method (c)*

This method is used widely in calculating one-dimensional energy spectra in three-dimensional isotropic turbulence. Assuming the turbulence to be isotropic, the values of the longitudinal velocity correlation coefficients $F(r)$, are defined by

$$F(r) = \frac{\overline{u_1(x)\,u_1(x+r)}}{\overline{u^2}}, \tag{5}$$

where u_1 denotes the velocity components parallel to the vector separation r. The velocity components $u(x)$ and $u(x+r)$ were obtained directly from projection of the particle streaks at x and $x+r$ on r. Here, $\overline{u^2}$ is defined by

$$\overline{u^2} = \frac{1}{N}\sum_{i=1}^{N} u_i^2, \tag{6}$$

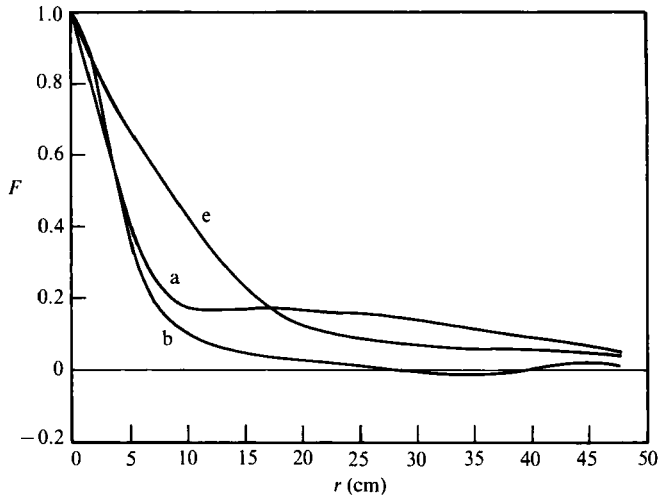for N particles. $F(r)$ was calculated for each particle pair in a given streak

FIGURE 7. Variation of the longitudinal velocity correlation function F as a function of separation r, for experiments a, b and e.
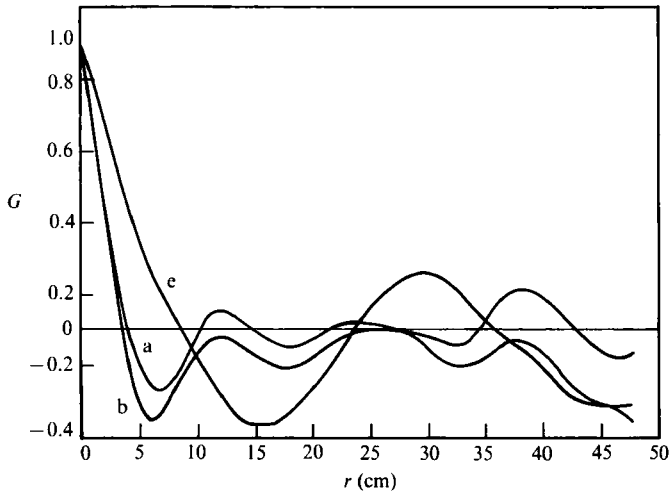

FIGURE 8. Variation of the lateral velocity correlation function G as a function of separation r, for experiments a, b and e.

photograph, and the results were averaged for a number of discrete bins in r. $F(r)$ is plotted for experiments a, b, and e in figure 7. Similarly, the values of lateral correlation coefficients $G(r)$ were calculated and plotted in figure 8. $G(r)$ is defined by

$$G(r) = \frac{\overline{u_2(x)\,u_2(x+r)}}{\overline{u^2}}, \tag{7}$$

where u_2 denotes velocity components perpendicular to vector separation r. Figures 7 and 8 indicate that the form of the functions $F(r)$ and $G(r)$ is typical of that predicted theoretically for two-dimensional turbulence (for example, see Townsend 1976, pp. 1–6).

The Fourier transform of the longitudinal correlation function $F(r)$ allows the $E(k)$ spectrum to be estimated and two examples appear in figures 9 and 10, for $\theta_* = 4$ and
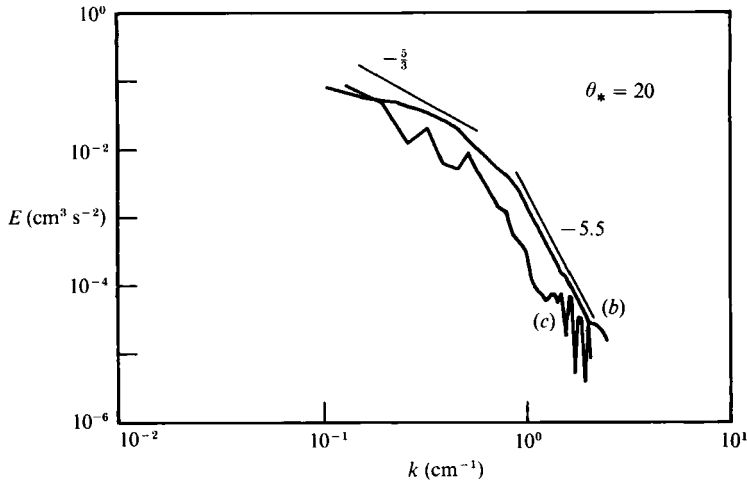
FIGURE 9. One-dimensional energy spectra E as a function of wavenumber k, calculated by (b) method (b), and (c) method (c) for experiment e.
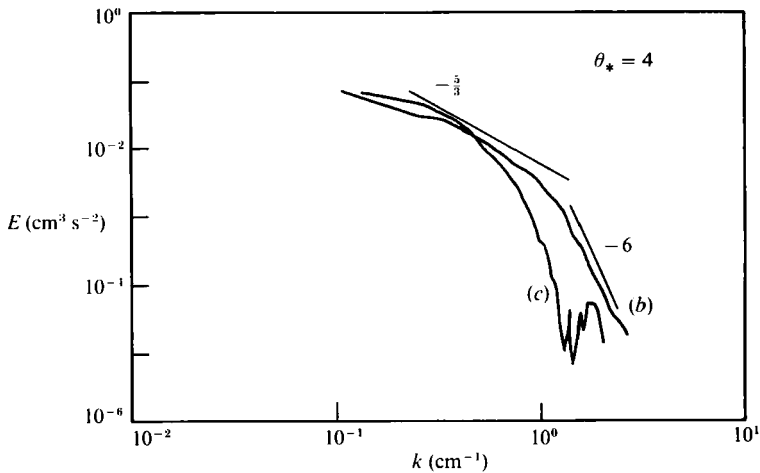

FIGURE 10. As in figure 9, but for experiment b.

20 (experiments b and e). The ringing of the data derived from the transformed correlation functions is a consequence of the spline interpolation of $F(r)$ preceding the transform operation and is hard to remove, but the upper envelope of this curve corresponds quite closely to the results from method (b). Hence, at wavenumbers $k < k_w$, the spectral slope generated using method (c) is consistent with $k^{-\frac{5}{3}}$, the inverse cascade inertia range. At wavenumbers $k > k_w$, method (c) did not produce well-correlated energy spectra when compared with the results generated by method (b), but in an average sense the spectral slopes are close to those that ($\sim k^{-5.5}$) given by method (b). The fact that methods (b) and (c) give similar decay laws to within experimental accuracy lends a degree of support for the interpolation procedures required for (b).

5.4 *The Kolmogorov constant*

It is possible to estimate the two-dimensional Kolmogorov constant (C) in the equation

$$E(K) = C\epsilon^{\frac{2}{3}}(k)^{-\frac{5}{3}}, \tag{8}$$

	A	ϵ	C	θ_*	R_t
a	0.5×10^{-2}	0.75×10^{-4}	2.8	1.7	340
b	0.5×10^{-2}	0.73×10^{-4}	2.86	4.0	460
c	0.52×10^{-2}	0.6×10^{-4}	3.4	7.5	660
d	0.5×10^{-2}	0.48×10^{-4}	3.8	11.0	511
e	0.5×10^{-2}	0.48×10^{-4}	3.8	20.0	830

TABLE 3.

where ϵ is the rate of energy injection to large scales. For the inverse cascade range, figure 5 gives an energy spectrum of the form

$$E(k) = A(k)^{-\frac{5}{3}}, \tag{9}$$

where the constant A can be determined directly from figure 5. Comparing (8) and (9) we find

$$C = \frac{A}{\epsilon^{\frac{2}{3}}}. \tag{10}$$

If the bottom layer is stationary (Narimousa & Maxworthy 1985), and the dissipation driving the Ekman layer is small compared with the dissipation at the interface, then the injected kinetic energy is dissipated mostly due to the action of molecular viscosity, and ϵ can be estimated from

$$\epsilon = 2\nu \int_0^\infty k^2 E(k) \, \mathrm{d}k \tag{11}$$

(see Batchelor 1953, §6.4 and Lesieur 1987, §5.3). Substituting (9) for $E(k)$ and integrating (11) within the range of wavenumbers in which figure 5 indicates the $k^{-\frac{5}{3}}$ inertia range, we find the value of ϵ and then from (10) the value of C. Table 3 shows the estimated values of A, ϵ and C for experiments a–e of figure 5, respectively. These values of C are within the range of those estimated by Lilly (1969), 4.3–6.2; Herring & Kraichnan (1975), 6.5; Herring & McWilliams (1985), 2.9–4.8; and Sommeria (1986), 3–7; but smaller than those of Frisch & Sulem (1984), 9; and much smaller than those of Siggia & Aref (1981), 14. The above table shows also the values of θ_* and $R_t = ul_i/\nu$, where $l_i \approx \lambda_w$ is the input wavelength, ν is the kinematic viscosity and u is the r.m.s. turbulent velocity.

6. Summary and conclusions

Fully developed, forced upwelling fronts and their associated frontal and pinched-off eddies were produced in a laboratory tank. Streak photographs of such a flow fields were digitized and recorded. To obtain the spectral distribution of kinetic energy a variety of statistical techniques were performed on the recorded data. The results of the computations are as follows:

(i) When particle dispersion methods were employed, both the relative velocity and the quadratic diffusivity measurements indicated energy spectra of the form $E \sim k^{-2 \pm 0.05}$ at higher wavenumbers. This spectral slope is much smaller than predicted by both the classical statistical theories and numerical simulations of two-dimensional turbulence, for the enstrophy cascade inertia range. The slope of energy spectra at lower k was consistent with $k^{-\frac{3}{2}}$, which was slightly less steep than predictions ($k^{-\frac{5}{3}}$) given by these same theories. Although these methods produced less steep spectral slopes, it appears that two inertial subranges were generated and more

importantly suggested that the input wavenumber was close to the wavenumber of the frontal eddies (k_w).

(ii) Direct two-dimensional Fourier transforms of the $u'^2(x, y)$-field were reduced to one-dimensional $E(k)$ spectra and produced two distinct inertial ranges also; a $k^{-\frac{5}{3}}$ spectrum at lower k and one approximately varying as $k^{-5.5}$ at higher k. The $k^{-\frac{5}{3}}$ result is consistent with that predicted for the inverse energy cascade inertia range, and the $k^{-5.5}$ is similar to those obtained in numerical simulations for the enstrophy cascade in stationary flows. The two inertial ranges meet close to a wavenumber that is associated with the wavenumber of the frontal eddies ($k_w \sim 2\pi(u_* f/g' h_0)$) so that k_w acts as the input wavenumber. However, these remarks should be judged cautiously since inspection of the vorticity and kinetic energy fields suggests that the high-wavenumber energy is associated with the relatively small-scale peaks of the vortex structures and probably not with any filamentary structures on the flanks of the vortices, which we cannot resolve, and which are usually thought to be responsible for the small-scale portion of the energy spectrum which evolves. By the same token, this further suggests that the usual notion of an enstrophy cascade in the fine filamentary structure around the flanks of the vortices should be viewed with some care.

(iii) $E(k)$ distributions derived from Fourier transforms of the one-dimensional longitudinal turbulent velocity correlations revealed spectra varying like $k^{-\frac{5}{3}}$ at lower k, which was in agreement with that obtained above. At higher values of $k > k_w$ the slope is consistent with the results shown in §5.2.

(iv) According to classical theories and numerical simulations of two-dimensional or geostrophic turbulence, the spectral slopes ($k^{-\frac{5}{3}}$ at $k < k_w$ and $k^{-5.5}$ at $k > k_w$) found in the present study suggest that turbulence in our model is two-dimensional. This in turn suggests that the prototype system that we are attempting to model can also be considered to be a two-dimensional turbulent field. Since jet-like structures evolve in such a field in the laboratory then presumably they do also in the natural flow: this helps to explain the filamentary structures which transport passive markers, e.g. heat, as observed in satellite images.

(v) We have estimated the two-dimensional Kolmogorov constant (C), within the $k^{-\frac{5}{3}}$ inertia range. The values of C varied within the range $2.8 < C < 3.8$, for a rather wide range of values θ_* and R_t. It appeared that slight increases in the value of C corresponded to an increase in the values of both θ_* and/or R_0.

REFERENCES

AGÜÍ, J. C. & JIMENEZ, J. 1987 On the performance of particle tracking. *J. Fluid Mech.* **185**, 447–468.

ARMI, L. & FLAMENT, P. 1985 Cautionary remarks on the spectral interpretation of turbulent flows. *J. Geophys. Res.* **90**, 11779–11782.

BABIANO, A., BASDEVANT, C. & SADOURNY, R. 1985 Structure functions and dispersion laws in two-dimensional turbulence. *J. Atmos. Sci.* **42**, 941–949.

BASDEVANT, C., LEGRAS, B., SADOURNY, R. & BELAND, M. 1981 A study of barotropic model flows: intermittency waves and predictability. *J. Atmos. Sci.* **38**, 2305–2326.

BATCHELOR, G. K. 1953 *The Theory of Homogeneous Turbulence.* Cambridge University Press.

BATCHELOR, G. K. 1969 Computation of energy spectrum in homogeneous two-dimensional turbulence. *Phys. Fluids Suppl.* **12**, II 233.

BENNETT, A. F. 1984 Relative dispersions: local and nonlocal dynamics. *J. Atmos. Sci.* **41**, 1881–1886.

BENNETT, A. F. & HAIDVOGEL, D. B. 1983 Low-resolution numerical simulation of decaying two-dimensional turbulence. *J. Atmos. Sci.* **40**, 738–748.

BRACHET, M. E., MENEGUZZI, M., POLITANO, H. & SULEM, P. L. 1988 The dynamics of freely decaying two-dimensional turbulence. *J. Fluid Mech.* **194**, 333–349.

BRACHET, M. E., MENEGUZZI, M. & SULEM, P. L. 1986 Small-scale dynamics of the high Reynolds number two-dimensional turbulence. *Phys. Rev. Lett.* **57**, 683–686.

BROWN, P. S. & ROBINSON, G. D. 1979 The variance spectrum of tropospheric winds over Eastern Europe. *J. Atmos. Sci* **36**, 270–286.

CHARNEY, J. G. 1971 Geostrophic turbulence. *J. Atmos. Sci.* **28**, 1087–1095.

CHIA, F. R., GRIFFITHS, R. W. & LINDEN, P. F. 1982 Laboratory experiments on fronts. Part II. The formulation of cyclonic eddies at upwelling fronts. *Geophys. Astrophys. Fluid Dyn.* **19**, 189–206.

DEEM, G.S. & ZABUSKY, N. J. 1971 Ergodic boundary in numerical simulations of two-dimensional turbulence. *Phys. Rev. Lett.* **27**, 396–399.

DUBOIS, M. 1975 Large-scale kinetic energy spectra from Eulerian analysis of Eole wind data. *J. Atmos. Sci.* **32**, 1838–1847.

FORNBERG, B. 1977 A numerical study of two-dimensional turbulence. *J. Comput. Phys.* **25**, 1–31.

FOX, D. G. & ORSZAG, S. A. 1972 Inviscid dynamics of two-dimensional turbulence. *Natl Center Atmos. Res. MS.* 72–80.

FRISCH, U. & SULEM, P. L. 1984 Numerical simulation of inverse cascade in two-dimensional turbulence. *Phys. Fluids* **27**, 1921–1923.

GAGE, K. S. 1979 Evidence for a $K^{-\frac{5}{3}}$ law inertial range in a mesoscale two-dimensional turbulence. *J. Atmos. Sci.* **36**, 1950–1954.

GRIFFITHS, R. W. & HOPFINGER, E. J. 1984 The structure of mesoscale turbulence and horizontal spreading at ocean fronts. *Deep-Sea Res.* **31**, 245–269.

GRIFFITHS, R. W. & LINDEN, P. F. 1981 The stability of vortices in a rotating stratified fluid. *J. Fluid Mech.* **195**, 283–316.

GRIFFITHS, R. W. & LINDEN, P. F. 1982 Laboratory experiments on fronts. Part I: Density driven boundary currents. *Geophys. Astrophys. Fluid Dyn.* **19**, 159–187.

HAIDVOGEL, D. B. & KEFFER, T. 1984 Tracer dispersal by midocean mesoscale eddies. I: Ensemble statistics. *Dyn. Atmos. Oceans* **8**, 1–40.

HERRING, J. R. 1980 Statistical theory of quasi-geostrophic turbulence. *J. Atmos. Sci.* **37**, 969–977.

HERRING, J. R. & McWILLIAMS, J. C. 1985 Comparison of direct numerical simulation of two-dimensional turbulence with two-joint closure: the effects of intermittency. *J. Fluid Mech.* **153**, 229–242.

HERRING, J. R., ORSZAG, S. A., KRAICHNAN, R. H. & FOX, D. G. 1974 Decay of two-dimensional homogeneous turbulence. *J. Fluid Mech.* **66**, 417–444.

HEYER, J. M. & SADOURNY, R. 1982 Closure modeling of fully developed baroclinic instabilities. *J. Atmos. Sci.* **39**, 707–721.

IMAICHI, K. & OHMI, K. 1983 Numerical processing of flow-visualization pictures – measurement of two-dimensional vortex flow. *J. Fluid Mech.* **129**, 283–311.

JULIAN, P. R., WASHINGTON, W. M., HEMBRE, L. & RIDLEY, C. 1970 On the spectral distribution of large-scale atmospheric kinetic energy. *J. Atmos. Sci.* **27**, 376–387.

KAO, S. K., JENNE, R. L. & SAGENDOLF, J. F. 1970 The kinetic energy of large-scale atmospheric motion in wavenumber-frequency space: II. Mid-Troposphere of the southern Hemisphere. *J. Atmos. Sci.* **27**, 1008–1020.

KILLWORTH, P. D., PALDOR, N. & STERN, M. 1984 Wave propagation and growth on a surface front in a two-layer geostrophic current. *J. Mar. Res.* **42**, 761–785.

KOLMOGOROV, A. N. 1941 Dispersion of energy in locally isotropic turbulence. *CR Acad. Sci. URSS* **32**, 16.

KRAICHNAN, R. H. 1967 Inertial ranges in two-dimensional turbulence. *Phys. Fluids* **10**, 1417–1423.

KRAICHNAN, R. H. 1975 Statistical dynamics of two-dimensional flow. *J. Fluid Mech.* **67**, 155.

LEITH, C. E. 1968 Diffusion approximation for two-dimensional turbulence. *Phys. Fluids* **11**, 671–673.

LESIEUR, M. 1987 *Turbulence in Fluids*. Martinus Nijhoff.

LILLY, D. K. 1969 Numerical simulation of two-dimensional turbulence. High-speed computing in fluid dynamics. *Phys. Fluid Suppl.* **12**, II 240.

LILLY, D. K. 1971 Numerical simulation of developing and decaying two-dimensional turbulence. *J. Fluid Mech.* **45**, 395–415.

LILLY, D. K. 1972 Numerical simulation studies of two-dimensional turbulence. I. *Geophys. Fluid. Dyn.* **3**, 289.

MAXWORTHY, T. 1989 The dynamics of two-dimensional turbulence. In *Proc. Conf. on the Oceanography of Sea Straits, les Arcs, France.*

MAXWORTHY, T., CAPERAN, P. & SPEDDING, G. R. 1987 Two-dimensional turbulence and vortex dynamics in a stratified fluid. In *Proc. Third Intl. Conf. on Stratified Flows. Pasadena, California.*

McWILLIAMS, J. C. 1984 The emergence of isolated coherent vortices in turbulent flow. *J. Fluid Mech.* **146**, 21–43.

MOREL, P. & LARCHEVEQUE, M. 1974 Relative dispersion for constant-level balloons in te 200 mb general circulation. *J. Atmos. Sci.* **31**, 2189–2196.

MORY, M. & HOPFINGER, E. J. 1986 Structure functions in a rotationally dominated turbulent flow. *Phys. Fluids* **29**, 2140–2146.

NARIMOUSA, S. & MAXWORTHY, T. 1985 Two-layer model of shear driven coastal upwelling in the presence of bottom topography. *J. Fluid Mech.* **159**, 503–531.

NARIMOUSA, S. & MAXWORTHY, T. 1986 Effects of a discontinuous surface stress on a model of coastal upwelling. *J. Phys. Oceanogr.* **16**, 2071–2083.

NARIMOUSA, S. & MAXWORTHY, T. 1987*a* Coastal upwelling on a sloping bottom: The formation of plumes, jets and pinched-off cyclones. *J. Fluid Mech.* **176**, 169–190.

NARIMOUSA, S. & MAXWORTHY, T. 1987*b* Effects of coastline perturbations on coastal currents and fronts. *J. Phys. Oceanogr.* **17**, 1296–1303.

NARIMOUSA, S. & MAXWORTHY, T. 1989 Application of a laboratory model to the interpretation of satellite and field observations of coastal upwelling. *Dyn. Atmos. Oceans* **13**, 1–46.

NARIMOUSA, S., MAXWORTHY, T. & SPEDDING, G. R. 1987 Structure of meso-scale baroclinic turbulence. *Sixth Symp. on Turbulent Shear Flows. Toulouse, France, September 7–9.*

NASTROM, G. D. & GAGE, K. S. 1983 A first look at wavenumber spectra from GASP data. *Tellus* **35**, 383–388.

PHILLIPS, N. A. 1954 Energy transformations and meridional circulations associated with simple baroclinic waves in a two-level, quasi-geostropic model. *Tellus* **6**, 273–286.

RIGNOT, E. J. M. & SPEDDING, G. R. 1988 Performance analysis of automated image processing and grid interpolation techniques for fluid flows. *University of Southern California, Department of Aerospace Engineering Internal Rep.* USCAE 143.

SAFFMAN, P. G. 1971 On the spectrum and decay of random two-dimensional vorticity distributions at large Reynolds numbers. *Stud. Appl. Maths* **50**, 377–383.

SALMON, R. 1978 Two-layer quasi-geostrophic turbulence in a simple case. *Geophys. Astrophys. Fluid Dyn.* **10**, 25–51.

SANTANGELO, P., BENZI, R. & LEGRAS, B. 1989 The generation of vortices in high-resolution, two-dimensional decaying turbulence and the influence of initial conditions on the breaking of self-similarity. *Phys. Fluids* A**1**, 1027–1034.

SIGGIA, E. D. & AREF, H. 1981 Point vortex simulation of the inverse cascade in two-dimensional turbulence. *Phys. Fluids* **24**, 171–173.

SOMMERIA, J. 1986 Experimental study of the two-dimensional inverse energy cascade in a square box. *J. Fluid Mech.* **170**, 139–168.

TOWNSEND, A. A. 1976 *Structure of turbulent Shear Flow*. Cambridge University Press.